Surface acoustic wave detection of robust zero-resistance states under microwaves

Jianli Wang,[1] L. N. Pfeiffer,[2] K. W. West,[2] K. W. Baldwin,[2] and Chi Zhang[3,4,1,5,*]

[1]*International Center for Quantum Materials, Peking University, Beijing 100871, China*

[2]*Department of Electrical Engineering, Princeton University, Princeton, New Jersey 08544, USA*

[3]*SKLSM, Institute of Semiconductors, Chinese Academy of Science, P.O. Box 912, Beijing 100083, China*

[4]*CAS Center for Excellence in Topological Quantum Computation, University of Chinese Academy of Sciences, Beijing 100190, China*

[5]*Collaborative Innovation Center of Quantum Matter, Beijing 100871, China*

(Received 29 March 2019; revised manuscript received 18 March 2020; accepted 20 March 2020; published 14 April 2020)

Microwave-induced resistance oscillations (MIROs) and zero-resistance states (ZRSs) occur in high-mobility two-dimensional electron gas exposed to microwave (MW). We observe that the velocity shift ($\Delta v/v$) oscillates in anticorrelation with MIRO, and $\Delta v/v$ shows peaks at the minimal resistance of MIRO or at ZRS. The SAW velocity features of ZRS remain robust even in the absence of external driving current, which suggests the involvement of intrinsic mechanism in the nonequilibrium phase. In addition, under high-power MW, the phase (φ_{ac}) of ZRS stays constant at about 1/4, whereas the phase of the transitions in MIRO is reduced to below 0.10. We argue that the peaks of SAW velocity at ZRS may result from the inhomogeneity of superposed current domain structures. Moreover, a multiphoton process around $\varepsilon = 1/2$ is observed in the SAW measurements.

DOI: 10.1103/PhysRevB.101.165413

I. INTRODUCTION

The high-mobility two-dimensional electron gas (2DEG) provides an ideal platform for the study of condensed matter physics. Under microwave (MW) irradiation, a different dissipative magnetoresistance oscillation, which is referred to as microwave-induced resistance oscillations (MIROs), is governed by the applied microwave frequency ω and cyclotron frequency ω_C [1,2], and the minima of MIRO are located at $\varepsilon \equiv \omega/\omega_C = n + 1/4$, where n is an integer number. In ultrahigh mobility 2DEG in GaAs/AlGaAs heterostructures, MW-induced zero-resistance states (ZRSs) occur at certain minimal regimes of MIRO [3,4]. Most experiments of MIRO are focused on electronic transport, other explored techniques include thermoelectric measurement [5], time-resolved capacitive measurement [6], field penetration method [7], and time-dependent photovoltage measurement [8]. Various mechanisms of MIRO have been proposed, such as the disorder-assisted inter-Landau-level transition in the displacement model [9,10], the MW-induced nonequilibrium steady-state (NESS) distribution in the inelastic model [11,12], the semiclassical model of microwave-driven time-dependent orbits [13], and the toy model of quantum tunneling junction [14]. MIRO is generally expressed as $\rho \propto -(\omega/\omega_C)P\lambda^2\sin(2\pi\omega/\omega_C)$, where P is the MW power, and λ is the Dingle factor. It is conventionally assumed that a negative resistivity appears at relatively large MW power in the MIRO minima [11]. ZRS emerges from spontaneously formed domain structures, as a result of the negative linear response conductance under microwave irradiation [9]. And each current domain has the current density j_0 much larger than the equivalent density of net current, but varies in direction and local electric field $E_{xx} = 0$ [12]. Direct experimental studies about the movement and formation of current domain, however, are still in need.

II. METHOD

The surface acoustic wave (SAW) technique offers a contactless, unidirectional, and conductivity-protective method to study the electron states coupled to piezoelectric materials. It has been successfully applied to researching the integer quantum Hall effects (IQHE) [15,16], the fractional quantum Hall effects (FQHEs) [17], the two-dimensional (2D) metal-to-insulation transition [18], and the Wigner crystal [19]. SAW serves as a complementary probe to detect the high-frequency response (i.e., high-frequency conductivity) of electron states. For example, the dc magnetoresistance (MR) dominated by the dissipationless edge state manifests properties of the ground state, whereas the SAW signals reveal the bulk electronic state of a sample regardless of the ground state. The experimental observation of nonequilibrium states under MW has stimulated ensuing theoretical reports [20,21]. In this study, we utilize SAW devices lithographically patterned on the sample surface to investigate microwave-induced nonequilibrium states.

III. RESULTS

Our samples of high mobility 2DEG come from the wafers with a 30 nm wide GaAs/AlGaAs quantum well (QW) that is located about 300 nm beneath the surface. The electron density is $n_e = 2.9 \times 10^{11}$ cm^{-2}, and the mobility is about $\mu = 3 \times 10^7$ cm^2/Vs after LED illumination at low temperature. A pair of interdigital transducers (IDTs) are deposited

*zhangchi@semi.ac.cn; gwlzhangchi@pku.edu.cn

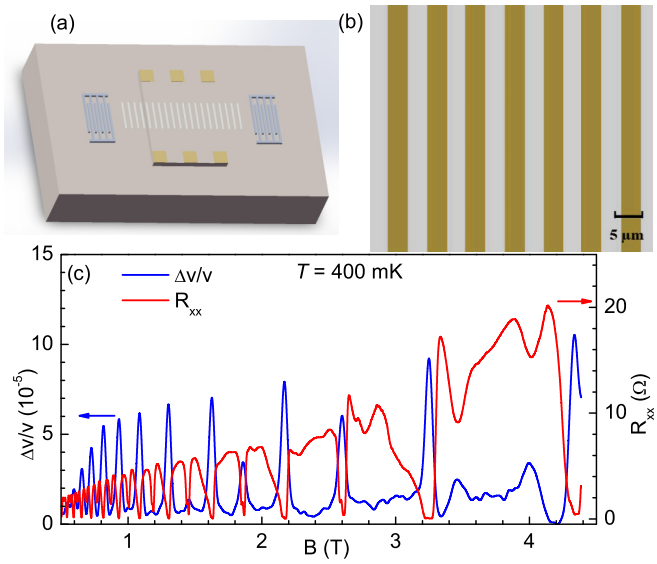

FIG. 1. (a) Schematic diagram of the experimental setup. The 2DEG is confined to a mesa by wet etching with an interaction length of 1 mm. A pair of interdigital transducers (IDTs) are fabricated on the etched area to excite and detect SAW signals on the sample surface. Six Ohmic contacts are arranged to detect the transport features. (b) Zoomed-in image of the IDT device. The interdigital periodicity is 16 μm. (c) Longitudinal resistance (red curve) and velocity shift (blue curve) versus B field at 400 mK.

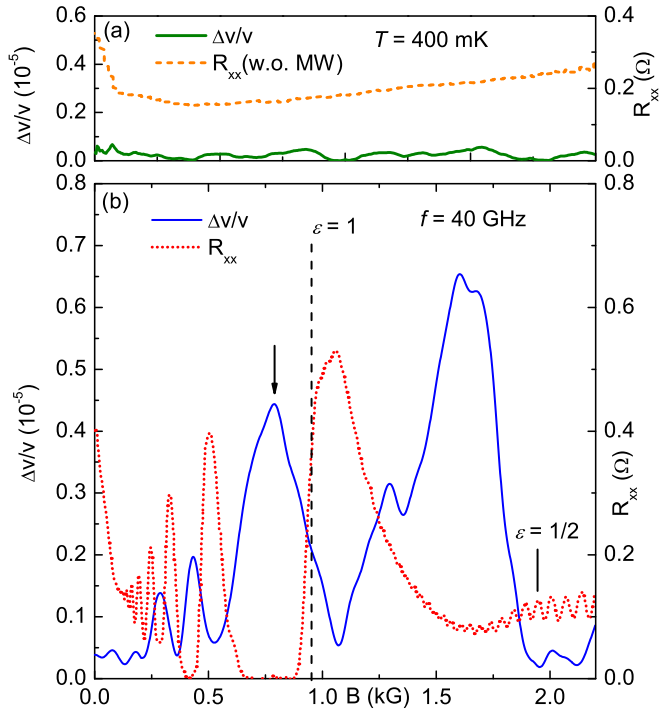

FIG. 2. Longitudinal resistance and velocity shift measurements of MIRO are carried out at 400 mK. (a) SAW velocity shift (olive color solid line) and R_{xx} (orange dashed line) without MW irradiation. (b) Under 40 GHz/15 dBm MW, the longitudinal resistance R_{xx} (red dotted line) exhibits $1/B$-periodic MIRO features, and distinct ZRS features emerge. The position of $\varepsilon = 1$ is denoted by the black dashed line. The velocity shift measurement (blue curve) is conducted simultaneously with the quasi-dc transport measurement. An evident velocity increase can be observed at the minima of R_{xx}. The indication of multi-photon process at $\varepsilon = 1/2$ is highlighted by a black short line.

on opposite sides of the mesa with an interaction length of 1 mm, as illustrated in Fig. 1(a). The designed period of IDTs is 16 μm, and the measured resonant frequency of the IDT device is about 180 MHz, thus the reference acoustic velocity is around 2880 m/s. Three ohmic contacts made of Ge/Pd/Au alloy are fabricated on each side of the 2DEG mesa along the SAW transmission direction, in order to obtain longitudinal and Hall resistance simultaneously with the standard quasi-dc technique. Along the surface of an elastic medium, SAW propagation is accompanied with both an elastic field and an electric field, which contributes to the interaction between SAW and 2DEG. Owing to the screening effect of 2DEG, the features of conductivity can be derived by monitoring the velocity shift of SAW. The SAW is generated and detected by a vector network analyzer (VNA) equipped with a time-gating option. A low power is applied to the IDTs, so that the results would not be affected by heating. To eliminate noises, we carry out SAW measurements under B fields with a very low B-sweeping rate of ~0.01 T/min. The acoustic wave experiments are conducted in a He-3 cryostat with a waveguide for MW irradiation and two coaxial cables. And the quasi-dc transport measurements are conducted simultaneously.

Figure 1(c) shows the traces of velocity shift ($\Delta v/v$) and longitudinal resistance (R_{xx}) as a function of perpendicular magnetic field (B) (without microwave irradiation) at 400 mK. The SAW velocity change exhibits a distinct anticorrelation with the sheet conductivity σ_{xx}, which is proportional to the longitudinal resistance R_{xx} in strong magnetic fields. When the Fermi level is located in the gap between two adjacent Landau levels (LLs), the electron states become less conductive and more incompressible, and R_{xx} displays Shubnikov-de Haas (SdH) oscillation (or IQHE) minima near the integer LL filling factors. Meanwhile, the SAW velocity at IQHE states manifests peaks, which indicates the insulating states in the bulk. Similarly, when the Fermi level is located in the center of a Landau level where the electron states turn conductive and compressible, the velocity falls back again. The velocity shift features of SAW ($\Delta v/v$) are almost quantitatively fitted with the relaxation model, which to a large extent depends on the magnetoconductivity σ_{xx}. The SAW velocity curves are plotted by removing the background, i.e., the velocity of electron states in 2DEG without MW.

The velocity shift can be expressed as:

$$\frac{\Delta v}{v_0} = \frac{\kappa_{\text{eff}}^2}{2} \frac{1}{1 + [\sigma_{xx}(q,\omega)/\sigma_m]^2}. \tag{1}$$

The effective coupling constant κ_{eff}^2 and the characteristic conductivity σ_m are determined by material and environment. The reference velocity v_0 is defined as the longitudinal propagation velocity in a medium, which can be perceived as the velocity in the nonpiezoelectric limit [16].

In order to probe the bulk properties of nonequilibrium states in 2DEG under MW irradiation, we apply the SAW method to study MIRO and ZRS. The blue curve in Fig. 2(b)

depicts the SAW velocity performance with a MW irradiation frequency of 40 GHz. For comparison, we show the zoom-in features of SAW and the transport data on 2DEG without MW in Fig. 2(a). There are no distinct features in either longitudinal resistance or SAW velocity in the low B-field regime without MW. In contrast, when exposed to MW irradiation, the longitudinal resistance R_{xx} [red dotted curve in Fig. 2(b)] exhibits strong MIRO and ZRS features under 40 GHz/15 dBm MW at 400 mK. The velocity changes of MIRO/ZRS with MW illumination are measured at the same time, shown by the blue curve. Compared with the velocity shift ($\Delta v/v$) without MW irradiation, which is denoted by the olive color curve in Fig. 2(a), distinct velocity oscillations can be observed when the ultraclean 2DEG is illuminated by MW, as is shown in Fig. 2(b). Similar to the results of IQHE displayed in Fig. 1(c), the SAW velocity with MW illumination manifests an increase at the MIRO/ZRS resistance minima regions, but falls back at the MIRO/ZRS resistance maxima regions. The $\varepsilon = 1$ ($\omega/\omega_C = 1$) cyclotron resonance position denoted by a black dashed line in Fig. 2(b) is slightly shifted to the negative magnetic field direction with respect to the MIRO resistance maximum position. The maxima and minima of MIRO and ZRS are located at $\varepsilon^{\pm} = n \mp \varphi_{ac}$, where n represents the order number of the cyclotron resonance harmonics and φ_{ac} is the phase factor. Quantitatively, the velocity peak of ZRS occurs at $B \sim 0.8$ kG, which corresponds to $\varepsilon = 5/4$ and $\varphi_{ac} = 1/4$, whereas the velocity minima of MIRO appear at $B \sim 1.07$ kG with $\varepsilon \sim 0.90$ and $\varphi_{ac} = 0.10$. Therefore, the velocity peaks coincide with the ZRS near $\varepsilon = n + 1/4$ or the resistance minima of MIRO, which agrees with the findings of magnetotransport experiments [23].

In addition to the velocity minima of the integer order of MIRO, we observe minima near $\varepsilon = 1/2$ in the SAW velocity plot [in Fig. 2(b)], which indicates the multiphoton process at relatively large MW power ($P = +15$ dBm). At the right-hand side of $\varepsilon = 1/2$, another minimum occurs at $\varepsilon \sim 0.454$ with a phase of $\varphi_{ac} = 0.5–0.454 = 0.046$, which corresponds to a maximum of the envelope in the Rxx trace. The minimum features at $\varepsilon \sim 0.5, 0.454$ appear at MW power higher than $+15$ dBm, and no obvious corresponding multiphoton process signals are observed in the longitudinal resistance plots. The phase φ_{ac} decays rapidly below 0.10 at high MW power in both cases of integer-order MIRO [23]. Similar behavior of phase occurs in the multiphoton process in our detection. Qualitatively, the up-to-date reported transport experiments of multiphoton process for MIRO are all below 30 GHz. But unexpectedly, the SAW measurements are very sensitive to the probing of the multiphoton process.

It is noteworthy that the SAW velocity features are preserved when the external current is removed from the measurements, as shown in Fig. 2(b), that is the SAW velocity manifests peaks at MIRO/ZRS resistance minima. A detailed description will be given later in Fig. 5(a).

The power-dependent SAW results of nonequilibrium states under 50 GHz MW irradiation are illustrated in Fig. 3. The magnetoresistance and velocity shift show similar patterns as those under 40 GHz MW, which are demonstrated in Fig. 2(b), disregarding the fact that the transmission efficiency of MW is a little weaker at higher frequencies. The minima of the velocity shift emerge at positions around $B \sim 1.3$ T, 0.63 T, 0.4 T, which are indicated by dashed lines. The minima of $\Delta v/v$ correspond to the maxima of R_{xx} at 50 GHz MW. With increasing input MW power, the SAW velocity features of MIRO/ZRS grow more distinct. In general, the intensity of the maximum velocity (at $\varepsilon \sim 5/4$) increases substantially with MW power. The features of $P = -10$ dBm are very weak and noisy. Only a wide peak around $\varepsilon = 5/4$ can be distinguished, whose quality is limited by the resolution in SAW measurements. The velocity features around the fillings $\varepsilon \sim 5/4, 9/4$, etc. change considerably with increasing input MW power from -10 dBm to $+10$ dBm. In particular, the peak intensity of ZRS increases dramatically around $\varepsilon = 5/4$, while the noises around the maximum smear out under high-power MW. The experimental results have no incompatibility with the theoretical and experimental reports that the current domain structure behaves more robustly with increasing microwave power. In short, the SAW features of MIRO and ZRS are congruent with the features of magnetotransport.

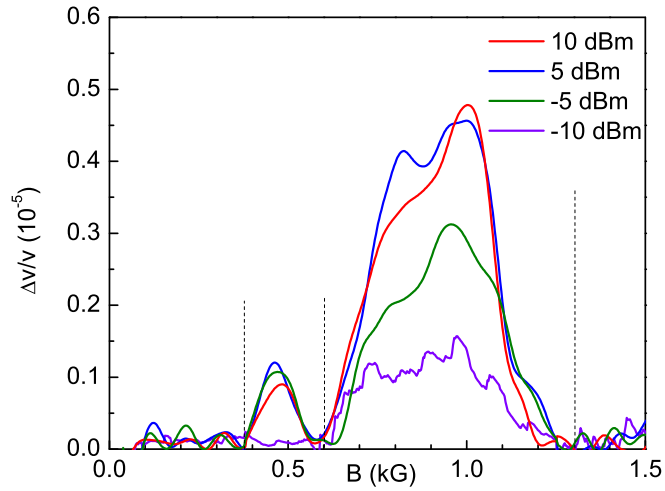

FIG. 3. Evolution of velocity shift ($f = 50$ GHz) at different input MW-power $-10, -5, 5, 10$ dBm, denoted by purple, green, red, and blue color respectively. The peak positions around $\varepsilon \sim 1, 2, 3$ in transport are highlighted by the dashed lines.

Quantitatively, we notice that the SAW minima positions ($\varepsilon^{+} = n - \varphi_{ac}$) of various nth-order MIRO are similar to those in transport [23], where the phase φ_{ac} depends on the nth order that is relevant to the separation of the LLs. Our observation of phase versus the nth order in SAW velocity is similar to that in transport. Meanwhile, the phase φ_{ac} decreases with increasing MW power, which is consistent with the results in transport study. At low MW power, the onset of the velocity minimum around $\varepsilon \sim 1$ moves to higher B fields ($B > 1.3$ kG). But at the highest MW power (10 dBm), the boundary of minimal velocity moves to lower B field. Based on our observation of the power dependence of acoustic velocity, the analysis of phase reduction supports the proposal of inelastic and displacement mechanism of MIRO [23].

We also investigate MIRO and ZRS under MW illumination at various frequencies. Figure 4(a) illustrates the traces of velocity shift versus B fields at frequencies ranging from 26–50 GHz, while the applied MW power is kept constant at 5 dBm. The velocity change for each trace of MW frequency exhibits intense peaks around $\varepsilon \sim 5/4, 9/4$, etc., which are

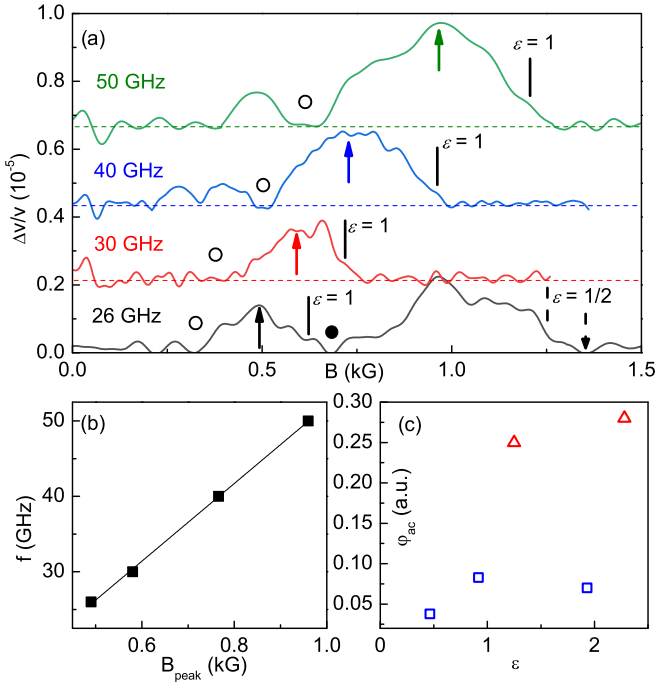

FIG. 4. (a) SAW velocity shift versus B field at various MW frequencies: ∼26–50 GHz. The traces are shifted vertically for clarity. The velocity shows a peak around MIRO minima or ZRS. The locations of $\varepsilon = 1$ are indicated by solid lines at various frequencies. The minima near $\varepsilon \sim 1$ are marked by solid circles, and the minima near $\varepsilon \sim 2$ are denoted by open circles. Notably, an extra minimum at 26 GHz is highlighted by a dashed arrow, which corresponds to the multiphoton process. The dashed line indicates the position of $\varepsilon = 1/2$ at 26 GHz. (b) The velocity peak positions marked by arrows in (a) show linear relations with MW frequency. (c) The relation of φ_{ac} vs ε shows that the phases of ZRS are close to 0.25 (red open triangles), and the phases of the nth-order transitions of MIRO are below 0.10 (blue open squares).

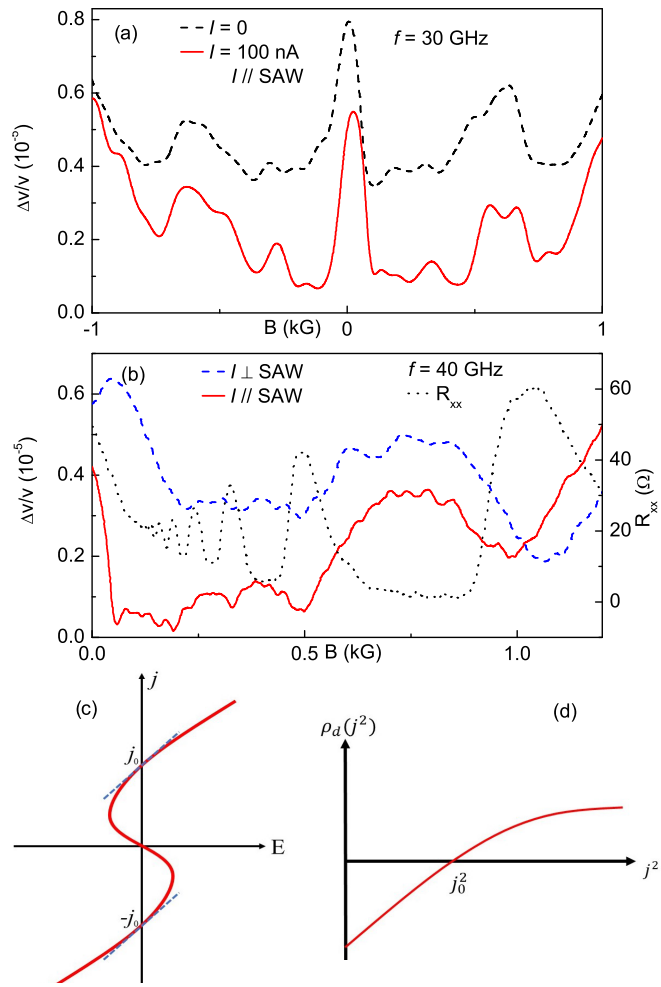

FIG. 5. The analysis of SAW velocity shift for nonequilibrium states under MW. (a) Comparison between configurations: (1) the SAW features without external current (black dashed line) and (2) the data with $I = 100$ nA parallel to the acoustic direction (red solid line). (b) Comparison between (1) the current parallel to SAW (red solid line) and (2) the current perpendicular to SAW (blue dashed line). The R_{xx} trace is illustrated with black dotted curve. (c) Dependence of the local E field on j in a current domain. The conductivity of each current domain region can be expressed as $\partial j_x/\partial E_x|_{j^2=0}$, as qualitatively represented with blue dashed line. (d) Dependence of the ZRS resistivity ρ_d on the square of the current j^2.

denoted by arrows. The peak position of the maximum around $\varepsilon \sim 5/4$ in B field is proportional to MW frequency [22,23], as shown in Fig. 4(b). On the right-hand side of ZRS in each trace, we indicate the positions of $\varepsilon = 1$ with solid lines, where a shoulder occurs. In the traces of 30, 40, and 50 GHz, MIRO competes with SdH oscillations at higher B, so the features of minima are not fully developed near $\varepsilon \sim 1$. On the contrary, the velocity minima near $\varepsilon \sim 2$ at low B are very distinct (denoted by open circles).

Due to the low MW attenuation, the features of MIRO at 26 GHz are more robust than in other traces. The velocity minima close to $\varepsilon \sim 1, 2$ are clearly evident. In addition, a velocity minimum of multiphoton process around $\varepsilon \sim 1/2$ is observed in the $f = 26$ GHz trace, which is highlighted by a black dashed arrow. The velocity minimum corresponds to the maximal resistance at the multiphoton process. According to Eq. (1), when the multiphoton process occurs the SAW velocity manifests a peak and σ_{xx} is zero. In our experiment, the multiphoton-process-induced magnetoresistance oscillations appear when the MW frequency is below 30 GHz. The result is consistent with previous reports that the multiphoton processes of MIRO are observed at MW frequencies below 30 GHz [24].

The dashed line [in Fig. 4(a)] highlights the position of $\varepsilon = 1/2$, and the velocity minima occur at $\varepsilon = 0.463$ (or $B = 1.35$ kG), whose corresponding phase is $\varphi_{ac} = 0.037$. Meanwhile, the integer-order minima of MIRO exhibit similar phases such as, $\varepsilon = 0.915$ ($\varphi_{ac} = 0.085$) of the first-order (solid circle), and $\varepsilon = 1.93$ ($\varphi_{ac} \sim 0.07$) of the second order (open circle). The relation of phase versus ε (at 26 GHz) is illustrated in Fig. 4(c): the phases of ZRS are denoted by red open triangles and the phases of the nth-order transitions are shown by blue open squares. The phases ($\varphi_{ac} < 0.10$) of transitions in MIRO are far from 1/4 under high-power MW, which supports the proposal of inelastic and displacement mechanisms [23].

Moreover, our observation shows that the SAW features are not pertaining to the external current. In Fig. 5(a), the SAW

velocity exhibits identical features when the external current is removed. The observation proves that the formation of the current domains is not related to the external driving current, but depends on the negative conductivity induced by MW irradiation. A supplement is shown in Fig. 5(b) to demonstrate the external driving current direction dependence. The SAW direction remains parallel to the x axis, whereas the direction of the external current varies. In both configurations of the current parallel to and perpendicular to the SAW propagation, we obtain the same features of SAW velocity.

In phenomenon, the SAW velocity of MIRO/ZRS behaves very similarly to that of IQHE (or SdH oscillations) shown in Fig. 1(c). The SAW velocity decreases at the maximal resistance position and increases at the minimal resistance position, which conforms to the SAW study in SdH oscillations. In general, the SAW oscillating features of MIRO can be attributed to the conductivity changes. And a distinct velocity increase at ZRS remains very robust. Although ZRS and IQHE both show zero conductance features macroscopically, they are fundamentally different in microscope. In IQHE regions, the magnetotransport is dominated by edge channels, and the homogeneous insulating bulk state has no contribution in transport. Hence the SAW velocity shows peaks when the conductivity exhibits minima. However, in ZRS regions, the composition will evolve into a state with inhomogeneous distribution of the current domains. According to the hypothesis of the dynamic current domains, a negative longitudinal conductivity appears at ZRS. The existence of negative conductivity leads to the instability of the electron state, thus the system spontaneously develops into current domain structures with a magnitude of the current $j = j_0$ in each current domain. The local dc-electric field $E = j\rho_d(j^2) + [j \times z]\rho_H$ evolves into $E = [j \times z]\rho_H$ with the direction perpendicular to the current, where ρ_d is the longitudinal resistivity of a single domain, and ρ_H is the transverse Hall resistivity. Based on the current domain picture, the conductivity of each current domain region can be extracted as $\partial j_x/\partial E_x|_{j^2=0}$, which remains positive as qualitatively presented in Fig. 5(c) with the external current aligned with the x axis. When the conductivity σ_{xx} for homogeneous system is replaced by the current domain conductivity $\partial j_x/\partial E_x|_{j^2=0}$ in Eq. (1), the high conductivity of the current domain is expected to cause no changes in the SAW velocity behavior of the ZRS region. Figure 5(d) illustrates the relation of $\rho_d(j^2)$ versus j^2. The current domain is fixed under the condition that the dissipative resistivity $\rho_d(j^2)$ equals zero.

IV. DISCUSSION

The effectiveness of the SAW velocity derivation [e.g., Eq. (1)] in the two-dimensional nonequilibrium states remains an open question in theory, for the behaviors of SAW velocity cannot be simply explained by the conductivity change model. Without experimental verification, the validity of SAW expression for nonequilibrium states in Eq. (1) is unexpected because the expression of σ_m for NESS differs from that in equilibrium states without MW irradiation. We try to provide a model to account for this situation. The interior of the areal sample at ZRS constitutes a dynamic inhomogeneous conducting domain structure [12]. Since the system consists of many current domains that are separated by domain walls, the average features of velocity shift can be ascribed to the superposed effects from current domains and domain walls. Another example related to the inhomogeneity in equilibrium states is about FQHE around $\nu = 2/3$ with spin transition. The inhomogeneity from the coexistence of domains and domain walls is analyzed by means of SAW [25]. In the time-dependent areal structure of ZRS, the domain walls display low conductivities, whereas the active current domains show high conductivities. Consequently, the increase of velocity shift at ZRS suggests the inhomogeneity from current domain structures. But an explicit theoretical expression about the SAW probing of the MW-induced current domain structures is still in need.

V. CONCLUSION

In summary, we provide the first experimental attempt to study MIRO and related ZRS by means of SAW, which aims to reveal the microscopic mechanism for the MW-induced nonequilibrium states in ultrahigh mobility 2DEG. The experiments show that the velocity oscillations of MIRO are anticorrelated with the feature's longitudinal resistance, and the robust velocity peak appear at ZRS. Under high-power MW, a phase reduction (below 0.10) occurs at the transitions of MIRO, but the phase of ZRS remains about 1/4. The contrast SAW study between MIRO and ZRS indicates different intrinsic mechanisms. The observation of MIRO supports the plausibility of inelastic and displacements models. And the study of ZRS in nonequilibrium suggests that the robust phase and intensity results from the superposed effect from current domain and domain walls. Therefore, SAW offers an effective method to characterize the bulk properties of MIRO and ZRS.

ACKNOWLEDGMENTS

We would like to thank Junren Shi for the helpful discussion. This project at Institute of Semiconductors, CAS and Peking University is supported by the National Science Foundation of China (Grants No. 11674006, No. 11974339) and by the National Basic Research Program of China (Grant No. 2014CB920904). The work at Princeton University is funded by the Gordon and Betty Moore Foundation through the EPiQS initiative Grant GBMF4420, and by the National Science Foundation MRSEC Grant DMR-1420541. J.W. and C.Z. conducted the experiments; J.W. and C.Z. analyzed data and wrote the paper; J.W. carried out the clean-room work for the devices; L.N.P., K.W.W., and K.W.B. grew the semiconductor wafers; and C.Z. conceived and supervised the project.

[1] M. A. Zudov, R. R. Du, J. A. Simmons, and J. L. Reno, Phys. Rev. B **64**, 201311(R) (2001).

[2] P. D. Ye, L. W. Engel, D. C. Tsui, J. A. Simmons, J. R. Wendt, G. A. Vawter, and J. L. Reno, Appl. Phys. Lett. **79**, 2193 (2001).

[3] R. G. Mani, J. H. Smet, K. von Klitzing, V. Narayanamurti, W. B. Johnson, and V. Umansky, Nature (London) **420**, 646 (2002).
[4] M. A. Zudov, R. R. Du, L. N. Pfeiffer, and K. W. West, Phys. Rev. Lett. **90**, 046807 (2003).
[5] A. D. Levin, G. M. Gusev, O. E. Raichev, Z. S. Momtaz, and A. K. Bakarov, Phys. Rev. B **94**, 045313 (2016).
[6] A. D. Levin, Z. S. Momtaz, G. M. Gusev, O. E. Raichev, and A. K. Bakarov, Phys. Rev. Lett. **115**, 206801 (2015).
[7] J. Mi, J. Wang, S. Fallahi, G. C. Gardner, M. J. Manfra, and C. Zhang, arXiv:1612.05196.
[8] S. I. Dorozhkin, L. Pfeiffer, K. West, K. von Klitzing, and J. H. Smet, Nat. Phys. **7**, 336 (2011).
[9] A. C. Durst, S. Sachdev, N. Read, and S. M. Girvin, Phys. Rev. Lett. **91**, 086803 (2003).
[10] M. G. Vavilov and I. L. Aleiner, Phys. Rev. B **69**, 035303 (2004).
[11] I. A. Dmitriev, M. G. Vavilov, I. L. Aleiner, A. D. Mirlin, and D. G. Polyakov, Phys. Rev. B **71**, 115316 (2005).
[12] A. V. Andreev, I. L. Aleiner, and A. J. Millis, Phys. Rev. Lett. **91**, 056803 (2003).
[13] J. Iñarrea and G. Platero, Phys. Rev. Lett. **94**, 016806 (2005).
[14] J. Shi and X. C. Xie, Phys. Rev. Lett. **91**, 086801 (2003).
[15] A. Wixforth, J. P. Kotthaus, and G. Weimann, Phys. Rev. Lett. **56**, 2104 (1986).
[16] A. Wixforth, J. Scriba, M. Wassermeier, J. P. Kotthaus, G. Weimann, and W. Schlapp, Phys. Rev. B **40**, 7874 (1989).
[17] R. L. Willett, M. A. Paalanen, R. R. Ruel, K. W. West, L. N. Pfeiffer, and D. J. Bishop, Phys. Rev. Lett. **65**, 112 (1990).
[18] L. A. Tracy, J. P. Eisenstein, M. P. Lilly, L. N. Pfeiffer, and K. W. West, Solid State Commun. **137**, 150 (2006).
[19] M. A. Paalanen, R. L. Willett, P. B. Littlewood, R. R. Ruel, K. W. West, L. N. Pfeiffer, and D. J. Bishop, Phys. Rev. B **45**, 11342 (1992).
[20] M. P. Kennett, J. P. Robinson, and N. R. Cooper, and V. I. Falko, Phys. Rev. B **71**, 195420 (2005).
[21] J. P. Robinson, M. P. Kennett, N. R. Cooper, and V. I. Falko, Phys. Rev. Lett. **93**, 036804 (2004).
[22] C. L. Yang, M. A. Zudov, T. A. Knuuttila, R. R. Du, L. N. Pfeiffer, and K. W. West, Phys. Rev. Lett. **91**, 096803 (2003).
[23] I. A. Dmitriev, A. D. Mirlin, D. G. Polyakov, and M. A. Zudov, Rev. Mod. Phys. **84**, 1709 (2012).
[24] M. A. Zudov, R. R. Du, L. N. Pfeiffer, and K. W. West, Phys. Rev. B **73**, 041303(R) (2006).
[25] D. Dini, R. B. Dunford, O. Stern, W. Dietsche, C. J. Mellor, K. von Klitzing, and W. Wegscheider, Phys. Rev. B **75**, 153307 (2007).